Remote sensing of flammable and toxic gases via IPDA lidar with InGaAs/InP single-photon detector over C + L band

HAOBIN HAN,¹ KEXIN GUO,¹ LI YI,¹ ZHEKAI LI,¹ JIADONG HU,^{1,4} SAIFEN YU,^{1,5,7} ZHEN ZHANG,^{1,5} TENGFEI WU,⁶ JIAWEI QIU,¹ AND HAIYUN XIA^{1,2,3,4,5,8} ®

Abstract: An integrated path differential absorption lidar (IPDA) for remote sensing of flammable and toxic gases is proposed, which is based on a broadband-tunable external-cavity diode laser (ECDL) and InGaAs/InP single-photon detector (SPD). An ECDL can maintain a narrow linewidth of 10 kHz throughout the continuous frequency scanning process in the C + L-band (1520-1620 nm), thus allowing a single laser to satisfy the detection requirements of multiple gases. To eliminate the influence of background light, a programmable frequency- and bandwidth-tunable grating filter is designed to synchronously tune with the output frequency of the ECDL. A homemade multi-channel coupled InGaAs/InP SPD maintains high detection efficiency in the C+L-band, ensuring the remote sensing detection capability of lidar. Four gases—CO, H¹³CN, C₂H₂, and NH₃—with absorption lines spanning ~45 nm in wavelength are selected to verify the multi-gas monitoring capability of the lidar. The intensity errors caused by erroneous photon counts and the non-linear frequency caused by the hysteresis effect of piezoelectric ceramic transducer are corrected to enhance the accuracy of absorbance spectra. The standard deviations of residuals between the experiment and single-peak fitting results for CO, H^{13} CN, C_2H_2 are 0.22%, 0.54%, 0.39%, while the mean deviations are 0.19%, 0.44%, 0.29%, respectively. For the four-peak fitting of NH₃, those values are 0.55% and 0.38%, respectively. Continuous 12-hour monitoring of the path-integrated concentrations of the four gases is conducted to verify the stability and accuracy of the system. The mean deviations and standard deviations of CO, H¹³CN, C₂H₂, and NH₃ are 0.13%, 0.13%, 0.02%, 0.17%, and 1.07%, 1.68%, 1.21%, 0.67%, respectively.

© 2025 Optica Publishing Group under the terms of the Optica Open Access Publishing Agreement

1. Introduction

Flammable and explosive gases leakage—such as methane (CH₄), hydrogen (H₂), hydrogen fluoride (HF), and acetylene (C₂H₂)—poses a significant risk of triggering fires or explosions, thereby threatening the safety of personnel and infrastructure [1–5]. Meanwhile, toxic gases leakage, including carbon monoxide (CO), hydrogen sulfide (H₂S), hydrogen cyanide (HCN), and ammonia (NH₃), directly imperil human health and may even cause acute poisoning or fatalities [6–10]. As such, the development of efficient monitoring equipment is imperative to

#572795 Journal © 2025

¹ School of Atmospheric Physics, Nanjing University of Information Science and Technology, Nanjing 210044, China

²State Key Laboratory of Climate System Prediction and Risk Management, Nanjing University of Information Science and Technology, Nanjing 210044, China

³School of Earth and Space Science, University of Science and Technology of China, Hefei 230026, China

⁴Institute of Lidar Technology, GuangZai Co. Ltd., Hangzhou 310005, China

⁵National Center of Carbon Metrology (Fujian), Nanping 353011, China

⁶Changcheng Institute of Metrology and Measurement, Aviation Industry Corporation of China, Beijing 100095, China

⁷sfyu@nuist.edu.cn

⁸hsia@ustc.edu.cn

enhance the surveillance and early warning of such hazardous gas leakage. Currently, the primary limitation restricting most existing gas leakage monitoring equipment to single-gas monitoring is the narrow wavelength tuning range of lasers, which renders it challenging to simultaneously cover the absorption lines of multiple gases. However, given the complex environments such as industrial production, combustion scenarios, and pollution emissions, the development of remote sensing equipment for flammable and toxic gases has become a critical technical requirement for ensuring production safety, environmental governance, and public health [11–13].

Passive detection technologies in multi-gas leakage remote sensing include passive optical gas imaging (OGI), passive remote sensing Fourier transform infrared spectroscopy (RS-FTIR), and spectral imaging technology [14–17]. These methods utilize the infrared radiation characteristics of gases or the environmental background to enable simultaneous monitoring of multiple gases. However, constrained by ambient optical interference, passive detection technologies face challenges in realizing continuous operation around the clock. Active detection works by emitting specific wavelengths related to gas absorption and inversely calculating gas concentrations based on the degree of laser intensity absorption by gases [18–21]. Distributed feedback (DFB) lasers are typically used as detection light sources in gas leakage monitoring due to the advantages of small size and high stability [22–26]. However, systems based on DFB laser are often only capable of detecting single gas due to the limitation of the narrow frequency tuning range. At present, integrating lasers and detectors of multiple frequencies is the main method for multi-gas leakage monitoring, the crosstalk between different frequencies is reduced by time-division multiplexing (TDM) or frequency-division multiplexing (FDM) [27-32]. However, the structure of multiple light sources and detectors often poses challenges such as complex architecture and difficult operation. External cavity diode laser (ECDL) diodes employing external cavity feedback technology can achieve continuous frequency tuning over a range exceeding 12 THz $(\sim 100 \text{ nm})$, while maintaining narrow linewidth characteristics during the tuning process [33–35]. Such wide-spectrum tunable light sources can effectively address the challenge that a single laser light source struggles to cover the absorption lines of multiple gases.

On the other hand, the performance of detectors plays a crucial role in the detection range of lidar systems. Detection signals undergo rapid attenuation through the atmosphere and scattering by non-cooperative targets in open-path scenarios, resulting in weak echo signal intensities. Single-photon detector (SPD) is a key technology to address this challenge, which can respond to single-photon energy levels [36–41]. Superconducting nanowire single-photon detectors (SNSPDs) exhibit ultra-high detection efficiency and low dark count rates under extremely low operating temperatures, which require complex and expensive cooling systems for maintenance [42–45]. Photomultiplier tube (PMT) has low noise, but the response bands are mainly in the ultraviolet-visible wavelength range [46–48]. InGaAs/InP single-photon avalanche diodes (SPADs) feature an all-fiber structure, miniaturization, and easy integration, with low requirements for working environments [49–52]. Since abundant gas absorption lines exist in response band of InGaAs/InP SPAD, which can be used to detect the gases leakage.

In past research, we have proposed CO₂ and HDO differential absorption lidar (DIAL) based on SNSPD [18,42], as well as CH₄ integrated path differential absorption (IPDA) lidar using InGaAs/InP SPD [50]. In this paper, an IPDA lidar with InGaAs/InP SPD over C + L band is proposed for remote sensing of flammable and toxic gases. The advantages of the proposed lidar are as follows: First, an ECDL can cover all gas absorption lines within the 1520-1620 nm range, enabling more flexible selection of absorption lines and avoiding errors caused by overlapping gas absorption lines. Second, a programmable grating filter is designed to effectively eliminate background light interference, thereby enabling the proposed lidar to achieve 24-hour continuous monitoring. Third, the InGaAs/InP SPD has the ability to detect ultra-weak light, supporting long-range remote sensing of gas leaks in open-path environments. CO, H¹³CN, C₂H₂ and NH₃ are selected to verify the multi-gas leakage monitoring capability of the proposed lidar

system. Experimental results demonstrate that the lidar exhibits excellent accuracy and stability. Compared with the structure using multiple light sources and detectors in traditional TDM technology, the wide-spectrum tunable device in this paper simplifies the system complexity.

2. System design and principle

The experimental setup diagram for multi-gas leakage monitoring lidar is shown in Fig. 1. Key parameters of the system are listed in Table 1. A commercial widely tunable ECDL (CTL 1550) with narrow-linewidth covering the C + L-band is used as the detection light source. The maximum frequency tuning range of the ECDL is limited by the gain spectral range of the gain chip in the active gain inner cavity. The frequency is stabilized by precisely controlling the temperature and current fluctuation of the ECDL. The output frequency of the ECDL is jointly controlled by an internal motor and a piezoelectric ceramic transducer (PZT). An arbitrary waveform generator provides a 50 Hz triangular wave modulation signal to drive the ECDL to operate in the frequency scanning state, thereby obtaining complete gas absorption lines. The laser energy is attenuated by a tunable optical attenuator to prevent the SPAD from saturation or breakdown. A transmitter with a diameter of 25 mm is used to collimate the laser and emits it into a gas cell with a 40 m optical path. A multi-gas calibrator is used to configure the gases to be measured. For safety considerations, H¹³CN is sealed in a standard gas cell with a 20 cm optical path and used to simulate the leakage of HCN. The partial beam reflected by the removable mirror with high-reflectivity is coupled into the PIN photodetector (PD) through a collimator. PIN PD serves as an ideal detector with negligible dead time (DT) and afterpulsing probability (AP), acting as a reference standard to verify the accuracy of the photon-counting correction. An oscilloscope with a bandwidth of 1 GHz is used for data acquisition. The transmitted part of light is diffusely scattered by a white cement wall 20 m away. The 20-meter detection distance used in the experiments is limited by the indoor experimental site. A receiver with a diameter of 50 mm couples the backscatter signal into a homemade programmable grating filter to eliminate the influence of background light.

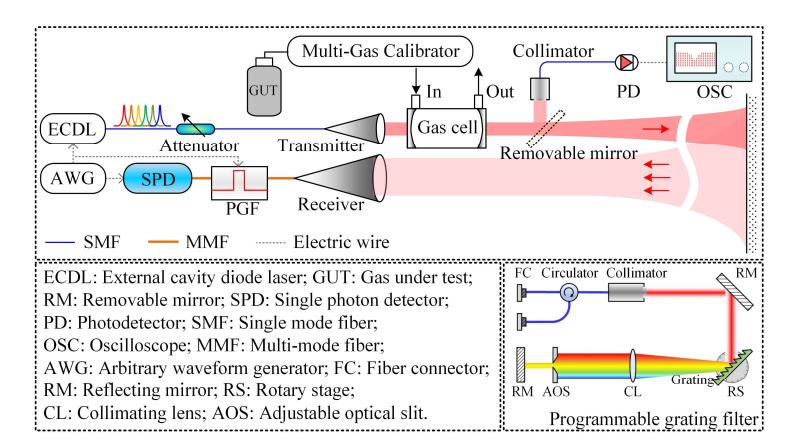


Fig. 1. Schematic diagram of the experimental system for multi-gas leakage monitoring lidar, and interior view of the programmable grating filter (inset, lower right corner).

As shown in the inset of Fig. 1, the programmable grating filter (PGF) receives and emits signals through a circulator. A grating fixed on a programmable high-precision rotation stage diffracts the input light that has been collimated and expanded by a collimator. According to the synchronous trigger signal sent by the AWG, the PGF quickly tunes the rotation stage to match the frequency of the ECDL based on the pre-calibrated grating angle related to the gas detection frequency. The diffracted light is collimated by a lens and incident onto a reflecting mirror, and

Table 1. Key parameters of the system^a

Sub-system		Parameter value
	Optical frequency span	185.06-197.23 THz/1520-1620 nm
ECDL	PZT scan	35 GHz
	Maximum power	25 mW
	Linewidth	10 kHz
	Max scan speed	10 nm/s
InGaAs/InP SPD	Detection efficiency	15%@1550 nm
	DT	200 ns
	AP	~12%
	DC	~500 cps
	Gate width	50 ns
Filter	Operating wavelength	186.21-197.23 THz/1520-1610 nm
	Bandwidth	3.7~370 GHz/0.03~3 nm
	Optical density	60 dB
	Tuning speed	20 nm/s

a "Optical density: $60\,\mathrm{dB}$ " refers to the filtering capability for out-of-band frequencies under specific frequency and bandwidth within the C+L band.

an adjustable optical slit in front of the reflecting mirror determines the bandwidth of the filter. A homemade multi-channel InGaAs/InP SPD is used to detect and analyze the filtered weak backscatter signal carrying gas concentration information.

Benefiting from the frequency-tunable wide-spectrum narrow-linewidth light source and wide-spectrum response InGaAs/InP SPD, the system can accurately detect all gas absorption lines within the C+L-band. This effectively overcomes the problem of insufficient detection of multiple gas absorption lines due to a narrow light source scanning range. H_2O and CO_2 are the two most dominant interfering gases in atmospheric gas detection, so the selection of gas absorption lines in open environments should minimize spectral overlap with these two gases. Additionally, the selected gas absorption lines need to have strong absorption cross-sections to enhance gas detection sensitivity. Using theoretical line parameters from the HITRAN database, the gas absorption cross-sections at 1 standard atmosphere and 296 K in the 180.598–197.233 THz range are simulated, as shown in Fig. 2 [53]. Four gases—CO, $H^{13}CN$, C_2H_2 , and NH_3 —are selected as analytes, the absorption lines of four gases with the wavelength span of \sim 45 nm.

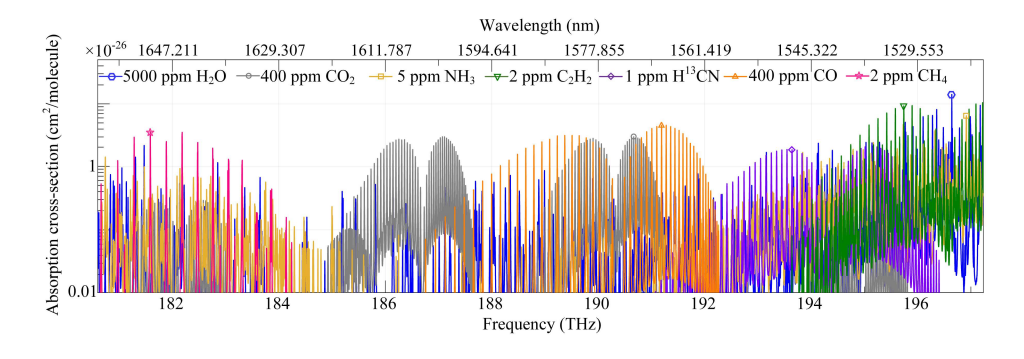


Fig. 2. Simulation of gas absorption cross-sections based on the HITRAN database.

The intensity $I(\nu)$ of laser after gas absorption can be described by the Beer-Lambert law, as shown in Eq. (1) [54]:

$$I(\nu) = I_0(\nu) \exp[-S(T)\phi(\nu)P\chi],\tag{1}$$

where $I_0(\nu)$ is the laser output intensity. S(T) represents the spectral line intensity at a specific temperature T, which is a crucial factor in selecting the laser output frequency and can be queried in the High-resolution transmission molecular absorption database (HITRAN). $\phi(\nu)$ is the normalized line profile function at a given pressure P and temperature. χ is the path-integrated gas concentration. In the experiment, the laser output frequency is tuned to scan the complete gas absorption cross-section. According to the measured $I_0(\nu)$ and $I(\nu)$, the absorbance spectrum $\alpha(\nu)$ of the gas to be measured can be expressed as:

$$\alpha(\nu) = -\ln[I_0(\nu)/I(\nu)]. \tag{2}$$

A suitable profile function is selected to fit the absorbance spectrum measured in the experiment. For a mixed absorbance spectrum composed of multiple absorption lines, a multi-peak fitting method can be employed for spectral separation. By integrating the fitted spectrum, the path-integrated concentration of the gas under test can be estimated using the area method:

$$\chi = \int_{-\infty}^{\infty} \alpha(\nu) d\nu / [S(T)P]. \tag{3}$$

3. Experiment

3.1. SPD correction

DT, AP, and dark counts (DC) are the main error sources in the counting results of SPD, causing intensity discrepancies in absorption curves during gas detection. Through special calibration and correction processes, photon-counting errors caused by DT, AP, and DC can be effectively corrected, thereby obtaining accurate detection results [49]. Figure 3 presents the photon counts results with the time resolution of 1 s for CO, $\rm H^{13}CN$, $\rm C_2H_2$ and $\rm NH_3$ before and after photon-counting correction. The count rate of the single-channel SPD is maintained at 0.9 Mcps to ensure linearity and the accuracy of the SPD correction method. The results before and after photon-counting correction are compared with those detected by a PIN PD to verify the accuracy of the correction method. Figures 3(a1-a4) show the raw data and stepwise corrections for DT, AP, and DC. DT induces significant photon loss at high incident photon rates, leading to more missed counts at the wings of gas absorption lines compared to the line center. AP generates spurious counts, which are more pronounced at the absorption line wings under high photon flux. DC is minimized to ~500 cps during SPD optimization, thus having negligible impact on the absorption lines.

Absorbance curves before and after photon-counting corrections are calculated using Eq. (2) and compared with the reference results detected by PIN PD, as shown in Figs. 3(b1-b4). Compare with the uncorrected results, the results after photon-counting correction exhibit excellent agreement with the data detected by PIN PD, validating the accuracy of the photon-counting correction method. Figures 3(c1-c4) depict the error analysis between the SPD results before and after correction and the reference results. The differences after correction show symmetric distribution about the absorption peaks, which is due to the different sampling methods between the SPD and PIN PD [55]. The deviation of absorbance detected by SPD before and after photon-counting correction is listed in Table 2. The significant optimization of intensity errors demonstrates the effectiveness and accuracy of the photon-counting correction method.

3.2. Non-linear frequency correction

Frequency scanning of the ECDL is achieved by adjusting the voltage applied to the PZT. Due to the inherent hysteresis effect of PZT materials, the deformation magnitude of the PZT varies

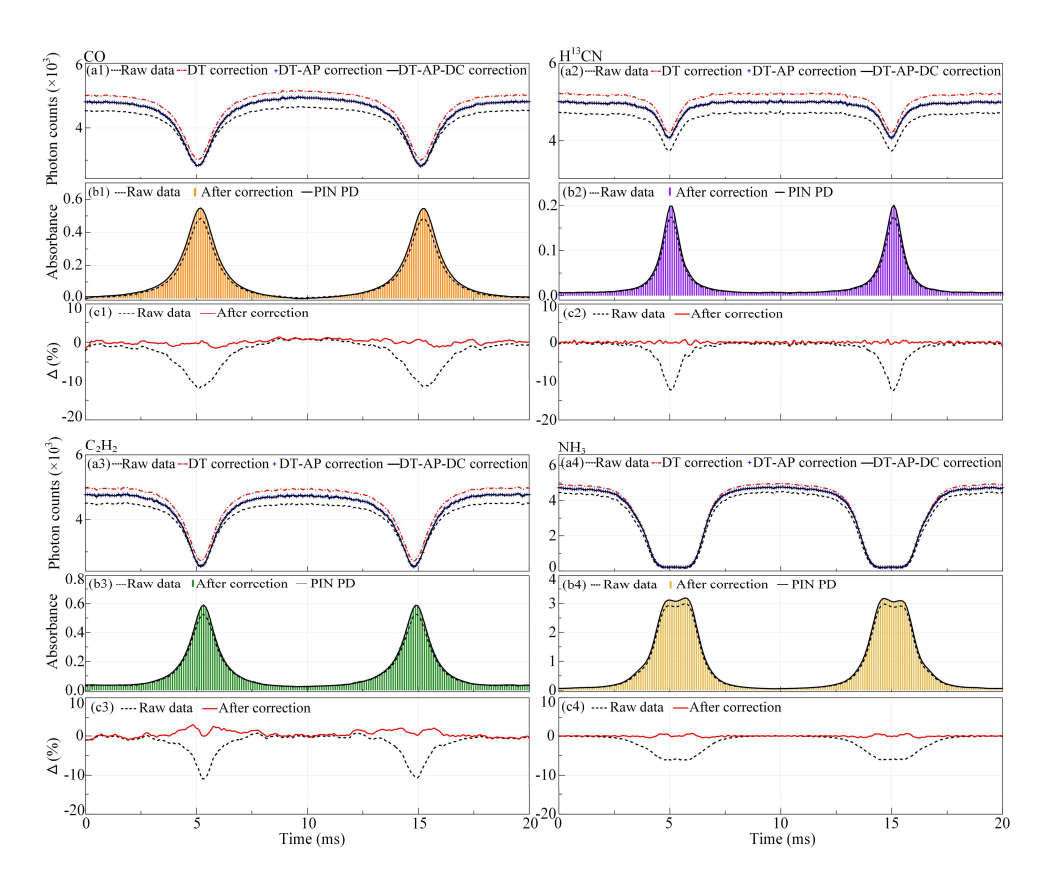


Fig. 3. The single-photon detection results for CO, $H^{13}CN$, C_2H_2 , and NH_3 , respectively. (a1-a4) Raw transmission signal and the results sequentially corrected for DT, AP and DC. (b1-b4) Comparison of absorbance detected by PIN PD and SPD. (c1-c4) Taking the results detected by PIN PD as a reference, the differences of absorbance using SPD before and after photon-counting correction. Each data point of SPD is accumulated by 2000 bins, corresponding to a cumulative time of $100~\mu s$. The time resolution is 1 s, and the photon counting rate of a single channel in the SPD is \sim 0.9 Mcps. Δ : difference.

Table 2. The deviation of absorbance detected by SPD before and after photon-counting correction

Formula	Deviation at the peak absorption (%)		Mean deviation (%)	
	Before correction	After correction	Before correction	After correction
CO	11.55	0.22	2.92	0.49
$\mathrm{H}^{13}\mathrm{CN}$	11.25	0.36	1.73	0.16
C_2H_2	10.91	0.41	1.75	0.70
NH_3	6.04	0.31	1.87	0.14

with the voltage sweeping direction (e.g., rising edge vs. falling edge) during the frequency scanning process. This further leads to non-linear frequency variations over time and distorts the measured absorbance spectrum. Figures 4(a-d) present the symmetry-calibration results of the absorbance spectra for CO, $H^{13}CN$, C_2H_2 and NH_3 without non-linear frequency correction. A clear asymmetry with larger deviations in the wings and smaller discrepancies at the absorption peaks is observed during up and down scanning. The maximum deviation for CO, $H^{13}CN$, C_2H_2

and NH_3 is 2.30%, 3.40%, 3.40% and 3.30%, respectively. The mean deviation for CO, $H^{13}CN$, C_2H_2 and NH_3 is 1.29%, 1.10%, 1.10% and 1.17%, respectively. These results underscore the necessity of correcting for non-linear frequency variations during laser scanning to improve the accuracy of gas absorption line measurements.

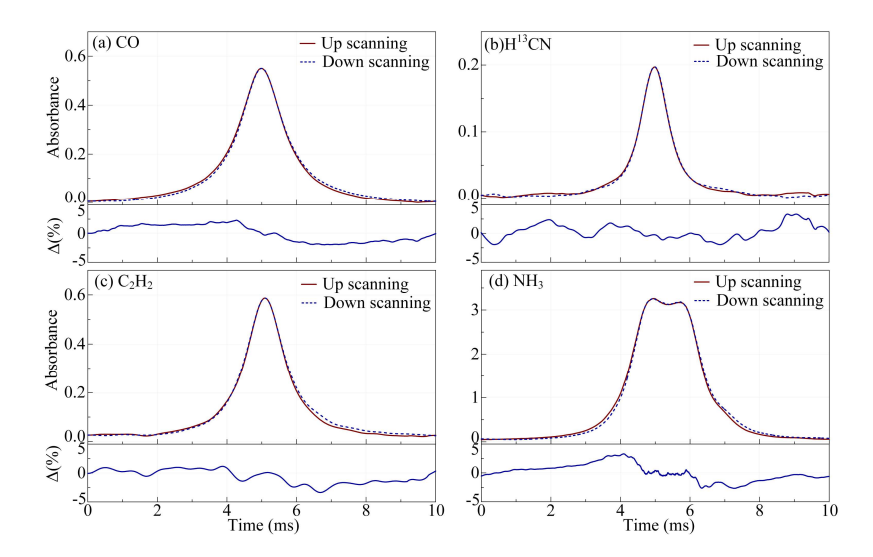


Fig. 4. Symmetry-comparisons of absorbance spectra before non-linear frequency correction during up and down scanning. (a) CO, (b) $\mathrm{H}^{13}\mathrm{CN}$, (c) $\mathrm{C}_{2}\mathrm{H}_{2}$, (d) NH₃. The subfigures below are the differences between the both absorbance spectra during up and down scanning.

In our previous work [47], joint time-frequency analysis (JTFA) was used for high spatiotemporal resolution signal processing of coherent Doppler wind lidar signals [56]. Meanwhile, the method combining homodyne detection with JTFA based on the Choi-Williams distribution enables accurate analysis and effective correction of non-linear frequency variations in DFB laser caused by current and temperature fluctuations [50]. Using the same approach, the non-linear frequency induced by PZT hysteresis during ECDL frequency scanning is corrected. Figure 5(a) shows the signal intensity distribution in time and frequency domains after JTFA of the homodyne detection signal. The black curve represents the maximum signal intensity at each time point, with the weakest intensity point corresponding to the gas absorption peak. By matching the gas species and ambient pressure, the true frequency at this point can be confirmed using the HITRAN database. As shown in Fig. 5(a), the value of frequency changes during up and down scanning are nearly identical at the gas absorption peak, resulting in good matching of the absorption curves at the peak position. However, significant frequency differences appear on both sides of the peak, causing temporal mismatches in the absorption curve wings and flanks. The frequency scanning range is obtained by integrating frequency changes at each time sampling point. Figure 5(b) represents that both up and down scanning covered a frequency range of ~35

Based on the time-frequency relationship analyzed by the JTFA, the non-linear frequency of absorbance spectra is corrected. A symmetric-calibration method is employed to compare the absorbance curves of the up and down scanning after non-linear-frequency correction, aiming to validate the accuracy of the non-linear frequency correction. Figure 6 presents the corrected absorbance spectra and corresponding errors for the four gases. The maximum and mean deviations for CO, $\rm H^{13}CN$, $\rm C_2H_2$ and $\rm NH_3$ are reduced to 0.52% and 0.17%, 2.68% and 0.80%, 1.32% and 0.47%, 0.58% and 0.10%, respectively. These results demonstrate that the combination

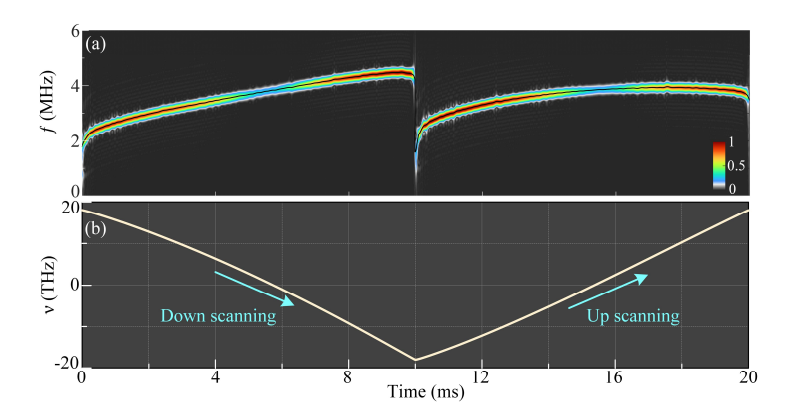


Fig. 5. (a) Homodyne detection signal f(t) processed by the JTFA with Choi-Williams distribution. (b) Relative optical frequency v during scanning.

of homodyne detection and JTFA effectively mitigates the non-linear frequency caused by PZT hysteresis in ECDL, thereby enhancing the accuracy of absorbance spectra measurements.

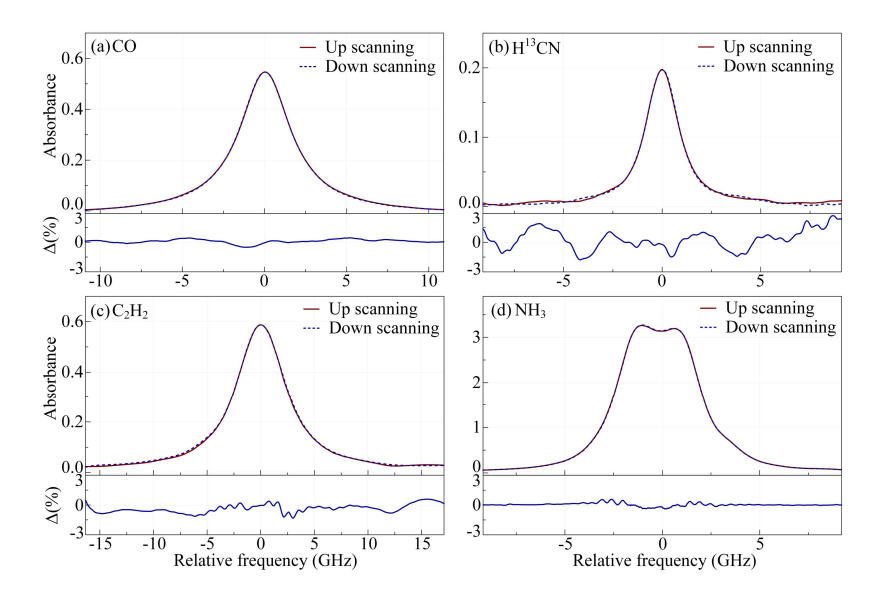


Fig. 6. Symmetry-comparisons of absorbance spectra after non-linear frequency correction in up and down scanning. (a) CO, (b) $\mathrm{H}^{13}\mathrm{CN}$, (c) $\mathrm{C}_2\mathrm{H}_2$, (d) NH₃. The subfigures below are the differences between the both absorbance spectra in up and down scanning.

3.3. Accuracy and stability

After correcting for intensity errors caused by erroneous photon-counting and non-linear frequency due to PZT hysteresis, the absorbance spectra of up and down scanning for each gas are averaged to serve as the fitting data. Voigt function is selected for fitting the absorbance spectra, and multi-peak fitting is performed on absorbance spectra composed of multiple absorption lines to separate overlapping spectral features. The fitting parameters of the four gases are listed in Table 3. The absorbance spectra of CO, $\rm H^{13}CN$, and $\rm C_2H_2$ each consist of a single absorption line within the frequency ranges of 191.179-191.201 THz, 193.631-193.650 THz, and 195.723-195.757

THz, respectively. The typical experiment results and corresponding Voigt fitting results of CO, $\rm H^{13}CN$, and $\rm C_2H_2$ are shown in Figs. 7(a-c). The standard deviations of residuals between the experiment and fitting result for CO, $\rm H^{13}CN$, $\rm C_2H_2$ are 0.22%, 0.54%, 0.39%, and the mean deviation are 0.19%, 0.44%, and 0.29%, respectively. The absorbance spectra of NH₃ consist of four absorption lines with the frequency range of 196.905-196.924 THz, while the experiment result and the multi-peak fitting result are shown in Fig. 7(d). The standard deviation and mean deviation of NH₃ are 0.55% and 0.38%, respectively.

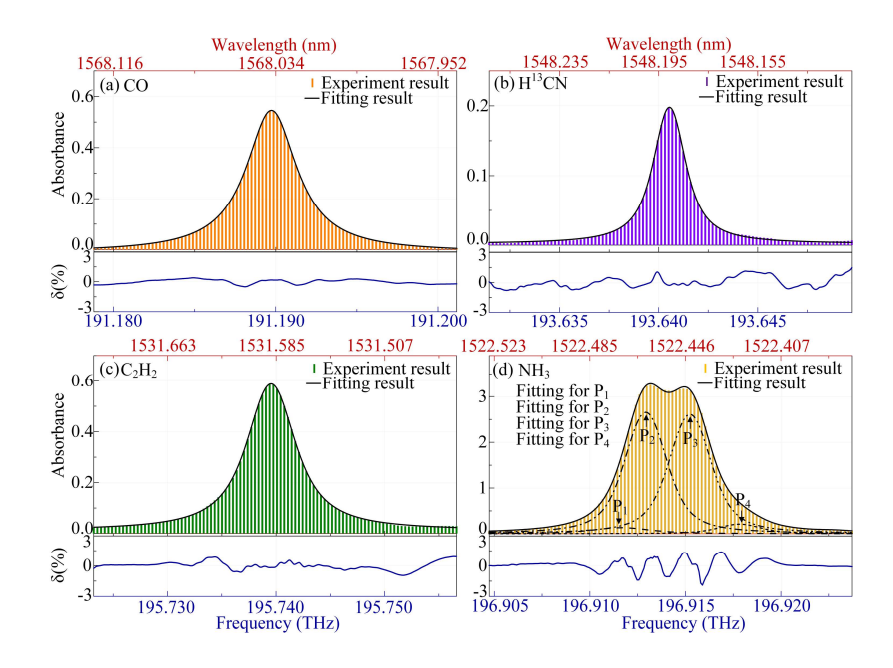


Fig. 7. Results of Voigt fitting for four gases. (a) CO, (b) $H^{13}CN$, (c) C_2H_2 , (d) NH_3 . The subfigures below (a-d) are residuals between the experiment and fitting results. δ : residual. P: absorption peak.

Table 3. Spectroscopic parameters of gases under test from HITRAN 2020^a

Formula	$ u/\lambda$	S	γ_{air}	γ_{self}	n_{air}	$E^{\prime\prime}$
CO	191.190/1568.034	2.251×10^{-23}	0.0606	0.066	0.75	107.6424
$H^{13}CN$	193.641/1548.187	6.252×10^{-21}	0.1102	1.183	0.79	103.6656
C_2H_2	195.740/1531.585	1.192×10^{-20}	0.0796	0.150	0.75	155.2890
NH ₃	196.912/1522.469	1.938×10^{-22}	0.0985	0.585	0.93	532.1009
	196.913/1522.461	2.571×10^{-21}	0.1072	0.600	0.73	85.0682
	196.916/1522.438	2.540×10^{-21}	0.1072	0.600	0.73	85.8644
	196.918/1522.423	2.058×10^{-22}	0.1031	0.364	0.69	0

 $^av(THz)/\lambda(nm)$: frequency/wavelength; $S(cm^{-1}/(molecule \cdot cm^{-2}))$: line intensity after natural abundance correction; γ_{air} and $\gamma_{self}(cm^{-1}/atm)$: air-broadened and self-broadened half width at half maximum (HWHM) at 1 atm and 296 K; $E''(cm^{-1})$: lower state energy of transition; n_{air} : coefficient of the temperature dependence of the air-broadened HWHM.

To further verify the stability of the proposed multi-gas leakage monitoring IPDA lidar, continuous 12-hour observations are conducted on the path-integrated concentrations of four gases, as shown in Fig. 8. The path-integrated concentrations for the calibration configurations

of CO, $\rm H^{13}CN$, $\rm C_2H_2$, and NH₃ are 1.65×10^6 ppm·m, 6×10^3 ppm·m, 6×10^3 ppm·m, and 1.35×10^5 ppm·m, respectively, with corresponding concentrations of 4.125×10^4 ppm, 1.2×10^3 ppm, 1.5×10^2 ppm, 3.375×10^3 ppm. The output power of the laser is attenuated to 1.9 mW, which corresponds to a signal intensity of \sim 5.4 Mcps. Figures 8(a-d) display 24 groups of test results for CO, $\rm H^{13}CN$, $\rm C_2H_2$, and NH₃ with a time interval of half an hour for each gas, where each group contains 10 results with a time resolution of 1 s. The mean deviations of CO, $\rm H^{13}CN$, $\rm C_2H_2$, and NH₃ are 0.13% (2145 ppm·m), 0.13% (7.8 ppm·m), 0.02% (1.2 ppm·m), and 0.17% (229.5 ppm·m), respectively. The standard deviations are 1.07% (17655 ppm·m), 1.68% (100.8 ppm·m), 1.21% (72.6 ppm·m), and 0.67% (904.5 ppm·m), respectively. The test results demonstrate that the multi-gas monitoring IPDA lidar exhibits good accuracy and precision.

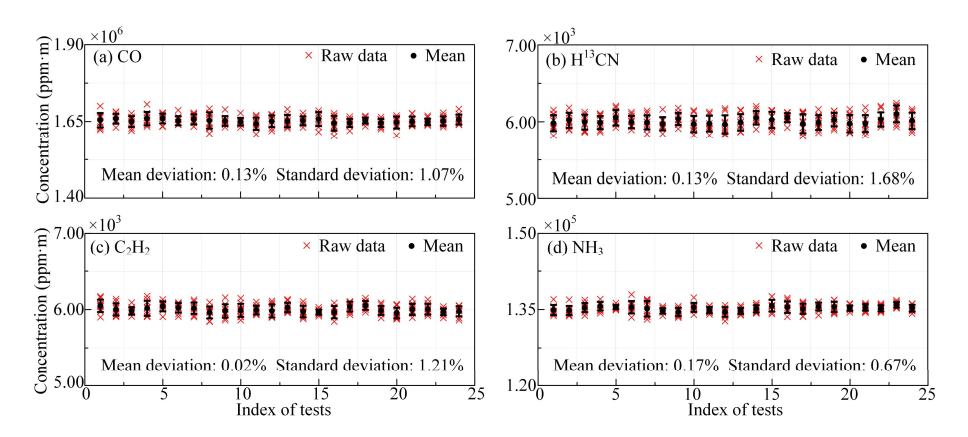


Fig. 8. 12-hour continuous observation of path-integral concentrations of (a) CO, (b) $\rm H^{13}CN$, (c) $\rm C_2H_2$ and (d) $\rm NH_3$. The output power of the laser is attenuated to 1.9 mW, which corresponds to a signal intensity of ~ 5.4 Mcps. The interval between each test group is half an hour, and each group contains 10 results with a time resolution of 1 s.

4. Conclusion

An IPDA lidar for flammable and toxic gases leakage remote sensing with single-photon sensitivity is proposed. An ECDL covering the C + L-band simplifies the traditional multi-laser configuration required for multi-gas detection. A programmable grating filter capable of synchronous tuning with the laser frequency effectively eliminates the influence of environmental noise, enabling the lidar to achieve 24-hour continuous monitoring. Four gases-CO, H¹³CN, C₂H₂, and NH₃-are selected to demonstrate the multi-gas leakage monitoring capability of the proposed lidar. The intensity errors caused by the DT, AP, and DC of the SPD and the non-linear frequency errors due to the hysteresis effect of the PZT have been corrected effectively. Firstly, the mean deviations of the intensity for the CO, H^{13} CN, C_2H_2 , and NH_3 are reduced from 2.92% to 0.49%, 1.73% to 0.16%, 1.75% to 0.70%, and 1.87% to 0.14%, respectively. Secondly, the non-linear frequency is corrected by combining the homodyne detection and JTFA, the symmetric-calibration method shows that the mean deviations of absorbance spectra at up and down scanning are reduced from 1.29% to 0.17%, 1.10% to 0.80%, 1.10% to 0.47%, and 1.17% to 0.10%, respectively. Finally, the Voigt function is used to fit the corrected absorbance spectra, and the path-integrated gas concentration is estimated using the area method. Continuous monitoring of four gases for 12 hours is conducted respectively to demonstrate the stability and accuracy of the system. The mean deviations and standard deviations of the path-integrated concentrations for the four gases are 0.13%, 0.13%, 0.02%, 0.17%, and 1.07%, 1.68%, 1.21%, 0.67%, respectively.

The preliminary experimental results demonstrate that the proposed IPDA lidar system for flammable and toxic gases leakage monitoring is reliable. In addition to CO, H¹³CN, C₂H₂, and NH₃ verified in this paper, the system can also monitor the concentrations of gases such as H₂O, CO₂, C₂H₄, and H₂S in the C + L-band. The accuracy of gas concentration is an important indicator. In photon counting systems, photon noise conforms to a Poisson distribution, and the system signal-to-noise ratio (SNR) is inversely proportional to the square root of the total photon count of the SPD [55,57]. Under ideal conditions—for example, when the DT, AP, DC, and environmental noise of the SPD are all corrected—the minimum error of the system can be estimated as 0.1% based on the total photon count of 1 mega count. The photon-counting correction will be further optimized to achieve correction accuracy when the SPD operates in the nonlinear response region, thereby improving the photon count rate and SNR. In path-integrated gas detection, the sensitivity of gas detection is related to the gas's absorption cross-section at a specific frequency and the integrated path length. The larger the gas absorption cross-section or the longer the integrated path length, the more significant the difference in photon attenuation, which in turn lowers the minimum detectable concentration of gas. In our subsequent work, we will investigate in detail the minimum detectable concentrations of the system for different gases.

Funding. National Natural Science Foundation of China (42305147, 42405138); Natural Science Foundation of Jiangsu Province (BK20230428).

Disclosures. The authors declare that there are no conflicts of interest related to this article.

Data availability. Data underlying the results presented in this paper are not publicly available at this time but may be obtained from the authors upon reasonable request.

References

- G. Han, Z. Pei, T. Shi, et al., "Unveiling Unprecedented Methane Hotspots in China's Leading Coal Production Hub: A Satellite Mapping Revelation," Geophys. Res. Lett. 51(10), e2024GL109065 (2024).
- K. Cai, X. Yang, S. Li, et al., "Accuracy Verification of Satellite Products and Temporal and Spatial Distribution Analysis and Prediction of the CH₄ Concentration in China," Remote Sens. 15(11), 2813 (2023).
- Y. Li, M. Bi, B. Li, et al., "Explosion hazard evaluation of renewable hydrogen/ammonia/air fuels," Energy 159, 252–263 (2018).
- 4. W. Duan, F. Yan, Y. Wang, et al., "A Laser-Based Multipass Absorption Sensor for Sub-ppm Detection of Methane, Acetylene and Ammonia," Sensors 22(2), 556 (2022).
- L. Wang, H. Ma, and Z. Shen, "Explosion characteristics of H₂/N₂O and CH₄/N₂O diluted with N₂," Fuel 260, 116355 (2020).
- X. Guo, F. Zheng, G. Li, et al., "A portable sensor for in-suit measurement of ammonia based on near-infrared laser absorption spectroscopy," Opt. Laser. Eng. 115, 243–248 (2019).
- Y. Wang, S. Chen, Q. Kong, et al., "Research on CO concentration detection based on deep learning and TDLAS technology," Opt. Laser. Eng. 181, 108420 (2024).
- 8. J. E. Duque, S. Lopez, and A. Molina, "Development of a tunable diode laser sensor for CO concentration analysis at laboratory-scale conditions for in situ combustion tests of heavy crude oils," Appl. Opt. **57**(23), 6707–6716 (2018).
- S. Ghanekar, G. P. Horn, R. M. Kesler, et al., "Quantification of Elevated Hydrogen Cyanide (H¹³CN) Concentration Typical in a Residential Fire Environment Using Mid-IR Tunable Diode Laser," Appl. Spectrosc. 77(4), 382–392 (2023).
- G. Li, H. Zhao, J. Li, et al., "A near infrared H₂S leakage detection system based on WDO-ELM using a digital lock-in amplifier combined with discrete wavelet transform filter," Infrared Phys. Techn. 128, 104481 (2023).
- 11. J. J. Nikkari, J. M. D. Lorio, and M. J. Thomson, "In situ combustion measurements of CO, H₂O, and temperature with a 1.58-µm diode laser and two-tone frequency modulation," Appl. Opt. **41**(3), 446–452 (2002).
- W. Weng, M. Alden, and Z. Li, "Simultaneous Quantitative Detection of HCN and C₂H₂ in Combustion Environment Using TDLAS," Processes 9(11), 2033 (2021).
- K. Zheng, L. Yu, C. Zheng, et al., "Vehicle-Deployed Off-Axis Integrated Cavity Output Spectroscopic CH₄/C₂H₆ Sensor System for Mobile Inspection of Natural Gas Leakage," ACS Sens. 7(6), 1685–1697 (2022).
- N. T. Vechi, J. Mellqvist, J. Samuelsson, et al., "Ammonia and methane emissions from dairy concentrated animal feeding operations in California, using mobile optical remote sensing," Atmos. Environ. 293, 119448 (2023).
- V. Selimovic, R. J. Yokelson, C. Warneke, et al., "Aerosol optical properties and trace gas emissions by PAX and OP-FTIR for laboratory-simulated western US wildfires during FIREX," Atmos. Chem. Phys. 18(4), 2929–2948 (2018).
- M. Kastek, T. Piątkowski, and P. Trzaskawka, "Infrared imaging fourier transform spectrometer as the stand-off gas detection system," Metrol. Meas. Syst. 18(4), 607–620 (2011).

- R. Y. Kang, P. Liatsis, and D. C. Kyritsis, "Emission Quantification via Passive Infrared Optical Gas Imaging: A Review," Energy 15(9), 3304 (2022).
- S. Yu, Z. Zhang, M. Li, et al., "Multi-frequency differential absorption lidar incorporating a comb-referenced scanning laser for gas spectrum analysis," Opt. Express 29(9), 12984–12995 (2021).
- W. P. Rosas and N. Cézard, "Greenhouse gas monitoring using an IPDA lidar based on a dual-comb spectrometer," Opt. Express 32(8), 13614–13627 (2024).
- S. Yu, D. Yu, Q. Xia, et al., "Spatiotemporal characteristics of atmospheric CO₂ under the influence of different industrial emission sources using lidar remote sensing in Nanping, China," J. Environ. Sci. 159, 490–501 (2026).
- H. Cui, F. Wang, Q. Huang, et al., "Multiparameter Measurement in Ethylene Diffusion Flame Based on Time-Division Multiplexed Tunable Diode Laser Absorption Spectroscopy," IEEE Photonics J. 11(3), 1–12 (2019).
- 22. G. Durry, J. S. Li, I. Vinogradov, et al., "Near infrared diode laser spectroscopy of C₂H₂, H₂O, CO₂ and their isotopologues and the application to TDLAS, a tunable diode laser spectrometer for the martian PHOBOS-GRUNT space mission," Appl. Phys. B 99(1-2), 339–351 (2010).
- F. Zhang, X. Qiu, L. Shao, et al., "Measurement of nitric oxide from cigarette burning using TDLAS based on quantum cascade laser," Opt. Laser Technol. 124, 105963 (2020).
- 24. M. Gu, J. Chen, J. Mei, et al., "Open-path anti-pollution multi-pass cell-based TDLAS sensor for the online measurement of atmospheric H₂O and CO₂ fluxes," Opt. Express 30(24), 43961–43972 (2022).
- J. Li, H. Deng, J. Sun, et al., "Simultaneous atmospheric CO, N₂O and H₂O detection using a single quantum cascade laser sensor based on dual-spectroscopy techniques," Sens. Actuators, B 231, 723–732 (2016).
- C. Roller, K. Namjou, J. Jeffers, et al., "Simultaneous NO and CO₂ measurement in human breath with a single IV–VI mid-infrared laser," Opt. Lett. 27(2), 107–109 (2002).
- J. Jiang, Z. Wang, X. Han, et al., "Multi-Gas Detection in Power Transformer Oil Based on Tunable Diode Laser Absorption Spectrum," IEEE Trans. Electr. Insul. 26(1), 153–161 (2019).
- M. Raza, Y. Chen, J. Trapp, et al., "Smoldering Peat Fire Detection by Time-Resolved Measurements of Transient CO₂ and CH₄ Emissions Using a Novel Dual-Gas Optical Sensor," Fuel 334, 126750 (2023).
- N. Liu, L. Xu, L. Zhang, et al., "Simultaneous Detection of Multiple Atmospheric Components Using an NIR and MIR Laser Hybrid Gas Sensing System," ACS Sens. 5(11), 3607–3616 (2020).
- 30. J. Sun, J. Chang, C. Wang, et al., "Tunable diode laser absorption spectroscopy for detection of multi-component gas: a review," Appl. Spectrosc. Rev. **59**(8), 1086–1107 (2024).
- 31. M. Raza, K. Xu, Z. Lu, *et al.*, "Simultaneous methane and acetylene detection using frequency-division multiplexed laser absorption spectroscopy," Opt. Laser Technol. **154**, 108285 (2022).
- 32. P. Fjodorow, M. P. Frolov, Y. V. Korostelin, *et al.*, "Room-temperature Fe: ZnSe laser tunable in the spectral range of 3.7-5.3 µm applied for intracavity absorption spectroscopy of CO₂ isotopes, CO and N₂O," Opt. Express **29**(8), 12033–12048 (2021).
- 33. G. B. Rieker, F. R. Giorgetta, W. C. Swann, *et al.*, "Frequency-comb-based remote sensing of greenhouse gases over kilometer air paths," Optica 1(5), 290–298 (2014).
- I. Bayrakli, "Tunable double-mode sensor for multi-gas detection based on the external-cavity diode laser," Appl. Opt. 57(15), 4039–4042 (2018).
- 35. A. Takamizawa, "Continuous frequency tuning of an external cavity diode laser significantly beyond the free spectral range by sweeping the injection current," Opt. Express 32(1), 774–784 (2024).
- A. McCarthy, N. J. Krichel, N. R. Gemmell, et al., "Kilometer-range, high resolution depth imaging via 1560 nm wavelength single-photon detection," Opt. Express 21(7), 8904–8915 (2013).
- 37. I. E. Zadeh, J. Chang, J. W. N. Los, et al., "Superconducting nanowire single-photon detectors: A perspective on evolution, state-of-the-art, future developments, and applications," Appl. Phys. Lett. 118(19), 190502 (2021).
- 38. R. Smith, A. C. Cardoso, I. Morland, et al., "Remote methane sensing using single-photon PPLN-waveguide upconversion lidar," Opt. Express 33(13), 28177–28188 (2025).
- R. H. Hadfield, J. Leach, F. Fleming, et al., "Single-photon detection for long-range imaging and sensing," Optica 10(9), 1124–1141 (2023).
- M. Shangguan, Y. Liang, Y. Li, et al., "Time-multiplexing single-photon imaging lidar with single-pixel detector," Appl. Phys. Lett. 124(5), 051104 (2024).
- 41. M. Shangguan, Y. Guo, and Z. Liao, "Shipborne single-photon fluorescence oceanic lidar: instrumentation and inversion," Opt. Express 32(6), 10204 (2024).
- S. Yu, Z. Zhang, H. Xia, et al., "Photon-counting distributed free-space spectroscopy," Light: Sci. Appl. 10(1), 212 (2021).
- V. Raj, A. Azem, M. Patterson, et al., "Waveguide integrated superconducting nanowire single-photon detectors for integrated photonics," J. Phys. D: Appl. Phys. 58(24), 243001 (2025).
- 44. M. Li, Y. Wu, J. Yuan, *et al.*, "Stratospheric aerosol lidar with a 300 μm diameter superconducting nanowire single-photon detector at 1064 nm," Opt. Express **31**(2), 2768–2779 (2023).
- B. Yue, S. Yu, M. Li, et al., "Local-scale horizontal CO₂ flux estimation incorporating differential absorption lidar and coherent doppler wind lidar," Remote Sens. 14(20), 5150 (2022).
- R. Foord, R. Jones, C. J. Oliver, et al., "The use of photomultiplier tubes for photon counting," Appl. Opt. 8(10), 1975–1989 (1969).

- 47. V. Yu. Glebov, C. Stoeckl, C. J. Forrest, *et al.*, "A novel photomultiplier tube neutron time-of-flight detector," Rev. Sci. Instrum. **92**(1), 013509 (2021).
- 48. M. Shangguan, Z. Yang, M. Shangguan, *et al.*, "Remote sensing oil in water with an all-fiber underwater single-photon Raman lidar," Opt. Express **62**(19), 5301–5305 (2023).
- 49. C. Yu, M. Shangguan, H. Xia, *et al.*, "Fully integrated free-running InGaAs/InP single-photon detector for accurate lidar applications," Opt. Express **25**(13), 14611–14620 (2017).
- H. Han, K. Wu, K. Guo, et al., "All-fiber IPDA lidar for CH₄ leakage monitoring using InGaAs/InP single-photon detector," Opt. Express 32(21), 37155–37166 (2024).
- 51. J. Titchener, D. Millington-Smith, C. Goldsack, *et al.*, "Single-photon Lidar gas imagers for practical and widespread continuous methane monitoring," Appl. Energy **306**, 118086 (2022).
- 52. P. Jiang, H. Xia, J. Hu, *et al.*, "Estimation of atmospheric refractive index structure constant using an InGaAs/InP single-photon detector," Opt. Lett. **48**(23), 6104–6107 (2023).
- I. E. Gordon, L. S. Rothman, R. J. Hargreaves, et al., "The HITRAN2020 molecular spectroscopic database," J. Quant. Spectrosc. Radiat. Transfer 277, 107949 (2022).
- A. Fathy, Y. M. Sabry, I. W. Hunter, et al., "Direct Absorption and Photoacoustic Spectroscopy for Gas Sensing and Analysis: A Critical Review," Laser Photonics Rev. 16(8), 2100556 (2022).
- 55. J. Qiu, H. Xia, X. Dou, *et al.*, "Optimization of scanning Fabry-Perot interferometer in the high spectral resolution lidar for stratospheric temperature detection," Opt. Eng. **55**(8), 084107 (2016).
- 56. C. Wang, H. Xia, Y. Liu, et al., "Spatial resolution enhancement of coherent Doppler wind lidar using joint time-frequency analysis," Opt. Commun. 424, 48–53 (2018).
- 57. H. Xia, D. Sun, Y. Yang, et al., "Fabry–Perot interferometer based Mie Doppler lidar for low tropospheric wind observation," Appl. Opt. 46(29), 7120–7131 (2007).